Functionalized Electrochemical Aptasensor for Sensing of Ochratoxin A in Cereals Supported by in silico Adsorption Studies

Kwanele Kunene, Myalowenkosi Sabela, Suvardhan Kanchi, Mikhael Bechelany, Krishna Bisetty

Functionalized Electrochemical Aptasensor for Sensing of Ochratoxin A in Cereals Supported by *in silico* Adsorption Studies

Kwanele Kunene[a,b], Myalowenkosi Sabela[a], Suvardhan Kanchi[a], Mikhael Bechelany[b*] and Krishna Bisetty[a*]

[a]*Department of Chemistry, Durban University of Technology, P.O. Box 1334, Durban 4000, South Africa*

[b]*Institut Européen des Membranes, IEM, UMR 5635, Univ Montpellier, ENSCM, CNRS, 34730 Montpellier, France*

Abstract

An aptamer to selectively detect ochratoxin A (OTA) in cereals was developed using silver nanoparticles (AgNPs) in combination with reduced graphene oxide (rGO). As a result of characterization experiments conducted in this study, AgNPs were confirmed to be polydisperse. The electro-catalytic activity was achieved by immobilizing OTA - bovine serum albumin (OTA - BSA) on the rGO/AgNPs substrate. Based on the experimental conditions optimized for the aptasensor, the linear dynamic range was 0.002 to 0.016 mg/L and the threshold was 7×10^{-4} mg/L (S/N = 3). At an atomic and molecular level, computational adsorption studies revealed how the OTA-BSA interacts with the rGO/AgNPs composite substrates on a spatial scale. Calculations using density functional theory (DFT) revealed that OTA has an energy gap of -4.5 eV, which implies a strong tendency to operate as an electron donor. In addition to its excellent reproducibility and good stability, the proposed aptasensor demonstrated its applicability in the food industry.

Keywords: *Ochratoxin A, AgNPs, reduced Graphene Oxide, electrochemical aptasensor*

[*]Corresponding authors: bisettyk@dut.ac.za (K. Bisetty),
mikhael.bechelany@umontpellier.fr (M. Bechelany)

1. Introduction

Ochratoxin A (OTA) is a metabolite produced by Penicillium and Aspergillus fungi that structurally consists of a chlorophenolic group containing a dihydroisocoumarin moiety that is linked to L-phenylalanine by an amide bond **(Figure S1A)**.[1, 2] It has a nephrotoxic, immunotoxic, teratogenic, mutagenic and carcinogenic effect in both animals and humans.[2, 3] As a common food contaminant, it enters the human body through the ingestion of inappropriately stored food products, such as alcoholic products, dried fruits, corn, coffee, spices and cereal products.[4-9] It is generally accepted that OTA is known to possess carcinogenic effects as stipulated by the International Agency for Research on Cancer (IARC).[10] For this reason, as part of the established regulations for OTA in foodstuffs, the European Commission established the maximum OTA levels for various foods such as spices (15-20 µg kg^{-1}), cereal products (3 µg kg^{-1}), dried fruits (10 µg kg^{-1}), soluble coffee (10 µg kg^{-1}), baby foods (0.5 µg kg^{-1}) and grape juices (2 µg kg^{-1}).[11-16] Many different analytical techniques are available for the detection of OTA. They include high performance liquid chromatography (HPLC)[17] thin layer chromatography (TLC),[18] liquid chromatography-mass spectroscopy (LC-MS),[19] gas chromatography-mass spectroscopy (GC-MS)[20] and enzyme-linked immunosorbent assays (ELISA).[21] Each of these generally acceptable methods has a limitation, such as low sensitivity, low limits of detection and the need for skilled personnel with expertise to handle high-end instrumentation. Notably they are costly, time-consuming and unable to meet the modern-day requirements with high selectivity, good precision, rapid analysis that is cost effective and easy to operate.

Aptamers are single-stranded DNA or RNA oligonucleotide fragments that bind to targets such as proteins, cells, small ions and molecules. These oligonucleotides are attained by an *in vitro* Darwinian method called single evolution of ligands by exponential enrichment (SELEX).[22] They have gained widespread recognition as probes for biomolecular detection, due to their convenient automated synthesis, high selectivity, stability, adaptable target binding and flexible modification with a variety of functional groups over antibodies.[23, 24] In recent years, several aptamer-based detection techniques for OTA including fluorescence,[25] colorimetry,[26] chemiluminescence[27] and electrochemistry[28] have been reported. There is increasing evidence which proves that the detection of OTA using electrochemical aptasensors is a powerful technique, due to fast response, high sensitivity, on-site testing platforms, low background noise, and good reproducibility.[29, 30] In a recent study by Lv and Wang 2020, they focused on

the signal amplification technologies applied to OTA electrochemical aptasensors and highlighted the current limitations and future challenges.[31] However, to design smart sensing for mycotoxins, it is crucial to synthesise highly efficient working electrode materials. As a result of their large specific surface areas, fast electron transfer, and high density of active sites, noble metal nanoparticles attract considerable research interest.[32] Specifically, AgNPs display an interesting quantum characteristics, large surface area, small particle diameter and it has the ability to transfer electron fast.[33] Therefore, AgNPs is widely used in the design of nanocomposites for electrochemical sensors.[1] Currently, numerous nanomaterials, such as carbon nanotubes (CNTs), noble metal nanoparticles and graphene oxide (GO) has been used to fabricate electrochemical sensors.[34-36] Previous reports revealed that GO and reduced graphene oxide (rGO) has been the key to such research, due to their distinctive properties including large surface area and high electrochemical conductivity.[37, 38] Several groups have studied the nanocomposite of graphene-metal nanoparticles for electrochemical sensors for detection of mycotoxins. Srivastava and co-workers have fabricated nickel nanoparticles (NiNPs) on rGO for the detection of aflatoxin B (AFB_1).[39] Shukla and co-worker have synthesized a reduced graphene oxide/tin oxide (rGO/SnO_2) nanocomposite for the detection of patulin in apple juice.[40] Jiang and co-workers reported a synthesis of gold nanoparticles and reduced graphene oxide (AuNPs-rGO) nanocomposite for the detection of OTA in wine samples.[41] However, the current literature review has not reported an aptamer-BSA combination fabricated with AgNPs on rGO for the detection of OTA. It was observed that there are no reports for the biosynthesis of AgNPs using amadumbe (*Colocasia esculenta*), a staple diet in the African continent, mainly South Africa, Nigeria and Kenya.[42] Thus, in this study, a bioinspired AgNP-based probe able to detect OTA using Amadumbe extract will be developed that is highly sensitive, cost-effective, and eco-friendly.

In the current study, a nanocomposite comprising of rGO/AgNPs as an electrochemical sensing material was used in conjunction with an aptamer-BSA complex for the design of a rapid and efficient OTA aptasensor. The signal amplification approach was achieved by anchoring the aptamer onto the surface of rGO/AgNPs and making use of the interaction effect of rGO and AgNPs fabricated onto carbon screen printed electrodes (C-SPEs). The C-SPE/rGO/AgNPs/Apt/BSA exhibited good electrocatalytic detection for OTA in food samples.

Motivated by the previous work done prompted a combined quantum mechanical and Monte Carlo simulations implemented to support the experimental methodology. Accordingly, the

electronic properties of the OTA in gas phase were investigated, using *ab initio* calculations based on density functional theory (DFT). An analysis of the adsorption phenomena of these electrode modifications has been carried out based on Monte Carlo simulations, which have helped to improve our understanding of important surface phenomena that cannot be determined just by experimentation.

To the best of our knowledge, the computational methodologies were performed in this study for the first time to assess the electronic and structural properties between the OTA and the BSA/Aptamer-nanocomposite. New insights into the interactions of OTA with the nanocomposite can help as a general regulatory guideline for sensing applications in the food industry.

2. Experimental section

2.1 Chemicals and reagents

The aptamer sequence 5′-GATCGGGTGTGGGTGGCGTAAAGGGAGCATCGGACA-3′, 5′-thionine[43] was purchased from WhiteSci, Whitehead Scientific (Pty) Ltd (Durban, SA). Amadumbe (*Colocasia esculenta*) and Weet-Bix purchased from a Durban supermarket. Standards of OTA, (1 mg/mL in dimethyl sulfoxide) and aflatoxin B_1 (AFB_1), 3.79 µg/g in acetonitrile were purchased from Sigma-Aldrich, Montpellier, France. Graphite powder, No.1 Whatmann filter paper, silver nitrate ($AgNO_3$), bovine serum albumin (BSA), chitosan (CS), potassium permanganate ($KMnO_4$), potassium ferricyanide $[Fe(CN)_6]^{3-}$, potassium ferrocyanide $[Fe(CN)_6]^{4-}$, sodium nitrate ($NaNO_3$, monosodium phosphate (NaH_2PO_4) and disodium phosphate (Na_2HPO_4) were purchased from Sigma-Aldrich, Durban, SA. Sulphuric acid (H_2SO_4) (97%, v/v), hydrogen peroxide (H_2O_2) (30%, w/w), hydrochloric acid (HCl) (37%, v/v) were purchased from Laboratory Supplies, Durban, SA.

2.2 Instrumentation

All UV–vis spectrophotometric measurements were performed with VARIAN Cary 50 spectrophotometer (South Africa) in the wavelength ranging 200 to 800 nm. *Colocasia esculenta* extract's functional groups and its role in the formation of nanoparticles were

analyzed using an attenuated total reflectance (Cary 630 FTIR Spectrometer from Agilent Technologies, SA) spectra from 200 to 4000 cm^{-1}. The particle size analysis of the biosynthesised AgNPs was performed using Single-particle ICP-MS (PerkinElmer NexION 2000 ICP-MS, Shelton, USA) equipped with the Syngistix nano software. The Asymmetric Flow Field Flow Fractionation (AF2000) equipped with MALS and UV–vis detectors from Postnova Analytics, Germany equipped with the AF2000 software was used for the separation and the hydrodynamic size distribution of the biosynthesized nanoparticles. The morphological characterization was carried with the high-resolution transmission electron microscopy (HR-TEM) using a JEOL ARM 200F high-resolution transmission electron microscope (200 kV) with an EDX analyzer (JED2300, at least 30 accumulations, matrix 512 × 512 points in STEM mode- X-Max, Oxford Instruments, Germany).

The electrochemical measurements were performed at room temperature with a portable combined bipotentiostat and spectrometer SPELEC Vis-NIR instrument from Metrohm SA. The three-electrode configuration comprised of a working electrode (WE), a counter electrode (CE) and a reference electrode (RE). The ProLab oven was used for drying purposes. A 781 pH/Ion meter from Metrohm SA was used for all the pH optimization measurements.

2.3 Synthesis of Graphene Oxide (GO) and Reduced Graphene Oxide (rGO)

In this work, GO was synthesized from natural graphite by slight modification of the Hummers' method.[44, 45] Approximately 1.2 g of graphite powder was oxidised by mixing with 2.0 g of $NaNO_3$ in 50 mL of concentrated H_2SO_4. The reaction mixture was stirred in an ice bath for 2 h, at a temperature range of 0-6 °C, and thereafter 6.0 g of $KMnO_4$ was gently added to the reaction mixture while stirring for another 2 h. Then it was removed from the ice bath and heated to 30 °C while stirring for a further 2 h during which the reaction mixture changed from black into a brownish paste. Then 8% of H_2O_2 was added into the reaction to weaken the paste. At this stage, the colour of the solution changed from brown to golden yellow, confirming the formation of GO. The resulting mixture was then centrifuged and washed 4 times with 8% HCl and deionized water respectively. Thereafter the filtrate was oven-dried and crushed into a fine powder. The reduced form of graphene oxide (rGO) was obtained by using chitosan as a reducing agent in the existing method. The conversion of GO to rGO was achieved with a 10 x dilution with chitosan (10.0 mg/mL in 1.0% acetic acid) under vigorous

stirring for 9 h at 90 °C.[46] The resulting product was then oven-dried at 40 °C for 48 h in order to obtain a powdered rGO.

2.4 Synthesis of Silver Nanoparticles (AgNPs)

The biogenic synthesis of AgNPs was conducted according to a previously reported method.[47] Fresh samples of amadumbe (*Colocasia esculenta*) as shown in **Figure S1B** were thoroughly washed with tap water, followed with deionised water, and cut into smaller pieces. To obtain the aqueous extract, 5.0 g of amadumbe pieces were boiled in 100 mL deionised water at 80 °C for 40 min and allowed to cool at room temperature. After cooling it was filtered through No.1 Whatmann filter paper. Different parameters such as boiling temperature of the extract, boiling time and the extracts amount were optimized for the complete reduction of silver. The filtrate was then used as the reducing agent for the synthesis of AgNPs by adding approximately 4.0 mL of 1.0 mM aqueous $AgNO_3$. The mixture was then stirred at 150 rpm for 30 min at 80 °C.

2.5 Preparation of rGO/AgNPs nanocomposite

The rGO/AgNPs nanocomposite was prepared by mixing 0.5 mg/mL of rGO and AgNPs in a ratio of 1:3 (v/v) in 50 mL of deionised water. The mixture was sonicated for 48 h to obtain a homogenized paste.

2.6 Fabrication of C-SPE/rGO/AgNPs/Apt/BSA aptasensor

The C-SPEs were first activated by applying a constant current of 3 μA for 2 min in 0.1 M H_2SO_4 solution rinsed thoroughly with MilliQ-water, and 0.1 M phosphate buffer at pH 7.0.[48] The activated C-SPE was coated by casting 10.0 μL of rGO/AgNPs paste and dried at 37 °C for 1 h. Thereafter 10.0 μL of 3.0 μM aptamer was dropped casted onto the rGO/AgNPs and dried at 24 °C, followed by washing with phosphate buffer to remove the excess (unabsorbed) aptamer from the C-SPE/rGO/AgNPs/Apt surface. Finally, the electrode was incubated with 1% (v/v) BSA solution for 20 min to completely block the unbound sites of the C-

SPE/rGO/AgNPs/Apt surface. The resultant OTA aptasensor electrode comprised of C-SPE/rGO/AgNPs/Apt/BSA (**Scheme 1**).

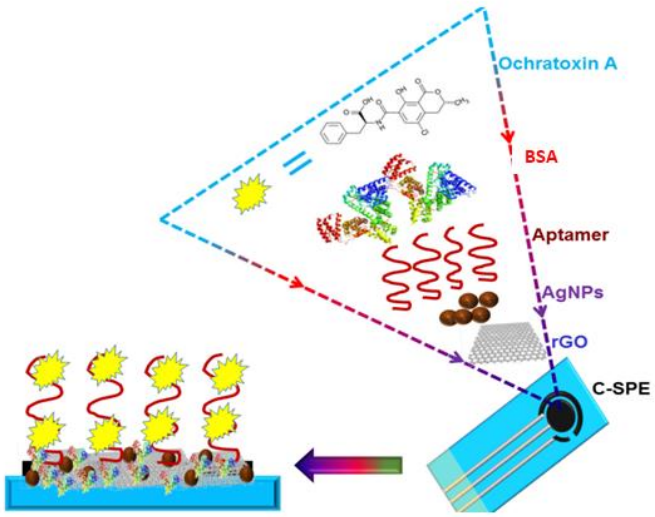

Scheme 1. Design of the electrochemical OTA aptasensor C-SPE/rGO/AgNPs/Apt/BSA.

2.7 Sample preparation

The non-contaminated Weet-Bix sample was prepared by following the procedure reported by He and co-workers.[49] An accurately weighed 4.0 g of the finely grounded sample was mixed with 10 mL methanol-PBS (60:40, v/v) and allowed to stand for 5 min under ambient conditions. The mixture was separated by filtration and the resulting methanol filtrate was spiked with different concentrations of OTA.

2.8 Characterization techniques

2.8.1 AF4-MALS

The biosynthesised nanoparticles were separated and characterized with an AF4-based system. The AF4 fractionation conditions are summarized in **Table S1.** AF4-MALS calibration was performed using polystyrene nanoparticle standard mixtures as described in a previous study.[50]

2.8.2 SpICP-MS

Single particle ICP-MS analyses were performed, operating in Standard mode as described in a previous study.[51-54]

2.8.3 TEM

Morphology studies were undertaken by transmission electron microscopy (TEM) as described in a previous study.[50]

2.9 Electrochemical measurements

The CV and DPV measurements were carried out in a redox probe of 1 mM $[Fe(CN)_6]^{3-/4-}$ containing 0.1 M PBS. All the electrochemical measurements were performed at room temperature in the potential range from -0.5 to 0.5 V.

3. Computational methodology

3.1 Density Functional theory (DFT) Calculations

Gaussian 09[55] was used to perform density functional theory (DFT) calculations on the geometrically optimized 3D structure of OTA (**Figure S1A**) using the 6–311+G basis sets. Further confirmation of the global minimum of the optimized geometry was obtained by calculating the frequency. An important parameter for defining chemical activity is the energy difference between the highest occupied molecular orbital (HOMO) and the lowest unoccupied molecular orbital (LUMO), with a smaller value denoting a stronger tendency to donate electrons. To confirm that the molecule has the ability to accept electrons in the LUMO, HOMO and LUMO plots have been computed.

3.2 Construction of the nanomaterials

A 3D model of the GO surface was constructed based on the MS software's standard structural database and features pristine graphite structures. Graphene oxide (GO) and silver

nanoparticles (AgNPs) are modeled using the Material Studio (MS) software package developed by BIOVIA.[56] For the AgNPs, a 3-D model is defined according to its standard structural database within MS. In order to assess their feasibility, an energy minimization procedure was conducted for each, followed by an optimization of geometry using a Forcite module with an ultrafine-COMPASS force field.[57] In this study, the maximum values of energy, force, stress, and displacement were set to be 2×10^{-5} kcal/mol, 0.001 kcal/mol, 0.001 GPa, and 10^{-5} Å respectively.

3.3 Molecular construction of the aptamer sequence

Based on the sequence, the secondary structure of ssDNA was built using M-fold, and refined equivalent 3D ssRNA models were constructed using Chimera, translated to ssDNA models by VMD.[58] The BSA (PDB code: 4F5S) structure was extracted from the protein database into MS to predict the interaction with the aptamer sequences. Discovery Studio visualizer was then used to explore the aptamer-BSA interaction. The selected aptasensor sequence was then synthesised by the local supplier.

3.4 Adsorption Studies by Monte Carlo Simulations

The lowest energy configurations of adsorbates on some selected substrates have been determined by Monte Carlo (MC) adsorption studies. By replicating the experimental layer-by-layer electrodes, the substrates and adsorbates were constructed (**Scheme 1**). Adsorption Locator (AL) functionality (MS software)[56] was used for each generated configuration, thereby showing the best adsorption sites. Analogues of the electrochemical layer-by-layer strategy were modelled by carrying out Monte Carlo simulations of the substrate–adsorbate conformational space since the temperature slowly decreased in accordance with a simulated annealing strategy during the adsorption process.[56,59]

Among the resulting adsorbate-substrate structures, the lowest adsorption energy conformers were each optimized for a stable conformation, and the adsorption energies are listed in **Table 2**.

4. Results and Discussion

4.1 Experimental section

4.1.1 Characterization of biosynthesized AgNPs

(i) AF4-MALS

The fractogram in **Figure 1A** represents the particle size distribution of AgNPs by AF4-MALS, under the optimised parameters indicating a clear separation from the void peak. The diameter of the particles (D_{geo}) for the elution time ranging from 10 to 25 min, results in the average geometric diameter of 55 nm.

(ii) spICP-MS

The spICP-MS was used to determine the size of the nanoparticles at low concentrations. The internal calibration with an isotope dilution was used to determine the size of AgNPs. **Figure 1B** revealed a size-based diameter, d = 48 nm.

(iii) TEM

The size, shape and morphology of AgNPs were identified using transmission electron microscopy (TEM). The TEM image (**Figure 1C**) confirms that the biosynthesized AgNPs are spherically shaped, with the average particle size of 53 nm. Veisi and co-workers reported a spherical shape of AgNPs, when they used plant extract as a reducing agent.[60] The TEM crystal lattice image (**Figure S1C**) shows the spherical nature of the particles that are highly crystallized; this is confirmed by the uniform lattice fringes. The lattice spacing of 0.23 nm corresponds to (111) planes of silver.

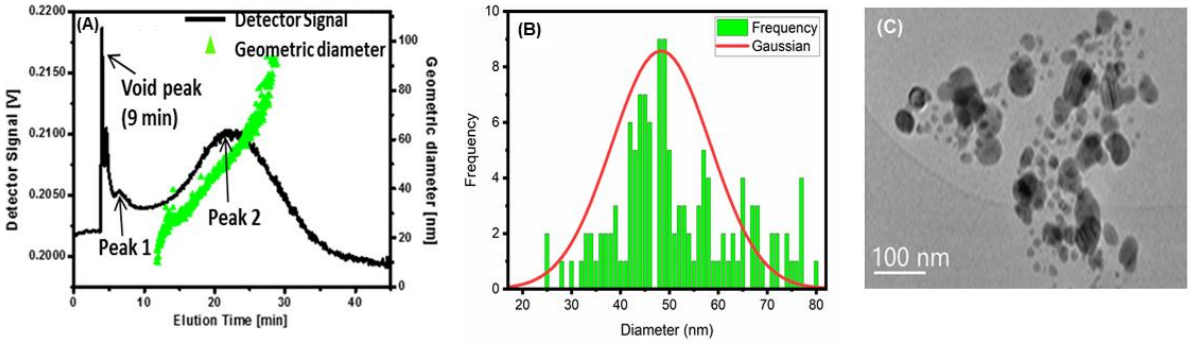

Figure 1. (A) AF4-MALS fractogram; (B) spICP-MS and (C) TEM images for biosynthesised AgNPs.

4.1.2 Spectroscopic characterization of rGO/AgNPs nanocomposite and C-SPE/rGO/AgNPs/Apt/BSA

(i) UV-Vis spectra

The reduction of Ag (I) to Ag (0) was observed by a colour change from colourless to brown and it was monitored by UV-Visible (**Figure S1D**). **Figure 2A** shows the UV-Visible spectra of (i) Amadumbe extract and (ii) AgNPs under the optimized conditions. The surface plasmon resonance (SPR) absorption band at 428 nm is observed, which is lower than that obtained by other researchers.[61, 62] This shows that the synthesized AgNPs are spherical in shape, in agreement with (TEM images in **Figure 1C**) and those reported by Alsharif et al (2020) and Ndikau et al (2017).[63, 64] The UV-Visible was also used for the characterization of GO and rGO. A distinct absorption band for GO was observed at 238 nm with a shoulder absorption band 298 nm (**Figure 2B**). These bands are associated with the $\pi \rightarrow \pi^*$ aromatic (C=C) and $n \rightarrow \pi^*$ (C=O) transitions, respectively. Similar results were reported in literature.[65-67] The absorption band of rGO red shifted to 265 nm depicting an accumulation of electrons and the removal of some functional groups on the GO surface.[66, 68, 69] The removal of oxygen and the C=O groups from GO results in the disappearance of the shoulder peak at 298 nm.[69]

(ii) ATR spectra

The ATR spectroscopy was used to identify the oxygen-containing functional groups that are present in the synthesised carbonaceous material. The ATR spectrum of GO and rGO (**Figure 2C**) shows an intense peak at 3586 cm^{-1}, corresponding to the O–H groups of the adsorbed water molecules between the GO sheets, demonstrating the hydrophilic characteristic of GO. The C=O stretching, aromatic C=C vibrations, epoxy C-O stretching vibration and the alkoxy C–O stretching vibrations were observed at 1731, 1625, 1245 and 1075 cm^{-1} respectively in the GO spectrum.[70-74] After the reduction of the GO, the peak at 1731 cm^{-1} disappeared, suggesting the elimination of the oxygen-containing functional groups, such as C=O and C-O bonds.[75, 76] The intense peak at 1591 cm^{-1} indicates the restoration of the sp^2 carbon networks.[77] The functional groups that are present in all fabrication steps of the aptasensor as shown in **Figure 2D**. The ATR spectra of C-SPE rGO/AgNPs shown in **Figure 2D (i)** is similar to that of rGO

but there is a weak intensity with a minor blue shift from 1585 to 1591 cm^{-1}, arising from the large presence of AgNPs.[78] After the immobilization of the aptamer onto the electrode surface, **Figure 2D (ii),** the C=O peak at 1645 cm^{-1} was observed, this confirmed the formation of metal-DNA aptamer bonding on the electrode surface.[79] The incubation of the blocking agent, BSA, on the electrode surface resulted in the secondary amide peak at 1532 cm^{-1}, indeed confirming the adsorption.

(iii) Raman Spectra

The Raman spectroscopy was used to characterize rGO before and after AgNPs were absorbed on the surface as shown in **Figure 2E**. The graphite spectrum is characterized by the G and D-bands. These two main bands are attributed to the disorder in the C-C bonds and the in-plane vibration bonds respectively.[80] The 2 characteristic D and G bands around 1320 cm^{-1} and 1586 cm^{-1} were observed on the rGO spectra before AgNPs modification (**Figure 2E (i)**). The D band provides information of the breathing mode of the k-point, while the G band relates to the tangential stretching mode of the E_{2g} phonon of the sp^2 carbon atoms.[81] After the AgNPs were decorated onto the rGO, the intensity of D and G bands observed at 1327 cm^{-1} and 1574 cm^{-1} respectively were then enhanced (**Figure 2E (ii)**) because of the surface enhanced Raman scattering of nanoparticles.

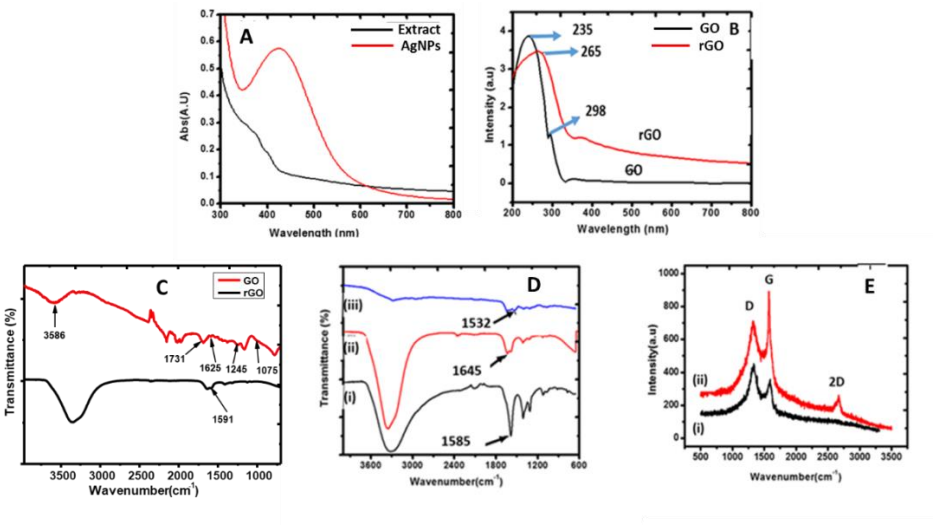

Figure 2. UV-Vis spectra of (A) AgNPs and Amadumbe extract, (B) GO and rGO; ATR spectra of (C) GO and rGO; and (D) (i) C-SPE/rGO/AgNPs, (ii) C-SPE/rGO/AgNPs/Apt, and (iii) C-SPE/rGO/AgNPs/Apt/BSA; and (E) Raman spectra of (i) rGO and (ii) rGO/AgNPs.

4.1.3 Electrochemical characterization of C-SPE/rGO/AgNPs/Apt/BSA

Cyclic voltammetry (CV) is one of the most useful techniques in the evaluation of the electrochemical behaviour of modified electrodes. **Figure 3** shows the cyclic voltammograms attained at the fabricated aptasensor in 5.0 mM $[Fe(CN)_6]^{3-/4-}$ prepared in a 0.1 M PBS buffer at pH 7. The bare C-SPEs displayed a well-defined redox peak which corresponds to the reversible redox reaction of $[Fe(CN)_6]^{3-/4-}$. After deposition of rGO/AgNPs composite, a significant increase in the redox peak current was observed, due to the presence of improved conductivity properties of rGO and AgNPs. The rGO/AgNPs composite promoted an electron transfer because of the increased surface area. The oxygen groups in GO provided a selective interface for the deposition of AgNPs. The π-π stacking interaction present in rGO accelerated the electron transfer and AgNPs conductivity.[82] After immobilization of the aptamer, a decrease in the redox peak suggests that the presence of the aptamer on the electrode surface hinders the electron transfer.[83] A further decrease in the peak current was observed on immobilization of BSA due to the blocking of the non-specific binding sites of the aptasensor, demonstrating a successful immobilization onto the electrode surface. The anodic peak potential (E_{pa}) shifts towards the left, while the cathodic peak potential (E_{pc}) shifts towards the right, this indicates an efficient mass transfer between the modified electrodes.[84]

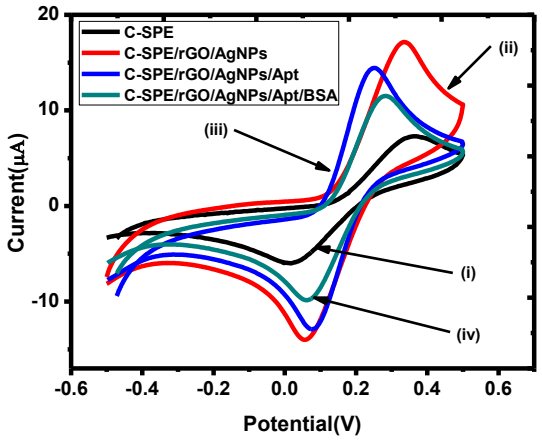

Figure 3. Comparative cyclic voltammograms of (i) bare C-SPE, (ii) C-SPE/rGO/AgNPs, (iii) C-SPE/rGO/AgNPs/Apt and (iv) C-SPE/rGO/AgNPs/Apt/BSA in 1 mM $[Fe(CN)_6]^{3-/4-}$ and 0.1 M PBS (pH 7.0) at a scan rate of 20 mV/s and (B) dependence of the peak potential shift at different electrode types.

4.1.4 Optimization of experimental conditions

In order to attain an outstanding analytical performance of the proposed aptasensor, the ratio, aptamer concentration, incubation time, incubation temperature, the OTA incubation time, and pH were optimized. The peak currents gradually increase with increasing rGO: AgNPs ratios (**Figure S2A**), because of the deposition of more metallic AgNPs with good electroactivity onto the modified electrode. The optimum value of the peak currents where observed at a ratio of 1:3, beyond which it decreases due to the reduction of the electron transfer efficiency. This is a significant result as it also limits the amount of aptamer immobilized onto the C-SPE/rGO/AgNPs surface.

The effect of the aptamer concentration was studied by modifying the electrode with concentrations ranging from 1 to 6 µM as shown on **Figure 4A**. The current response increases from 1 to 3 µM with a maximum of 37.5 µA, and thereafter decreases because of a poor interfacial electron transfer of the aptamer. The incubation time of the 3 µM aptamer was optimized by monitoring the current responses for 6 h (**Figure 4B**). There is an increase in current with increasing incubation time reaching a maximum of ΔI_{pa} at 3 h, beyond which it decreases due to a longer incubation time, resulting in the partial hybridization of the aptamer. Consequently, 3 h was selected as the optimum incubation time.

DNA has a specified working temperature due to the presence of different functional groups that may affect the incubation temperature when fabricating the aptasensor. **Figure 4C** shows an increase in ΔI_{pa} results in an increase of the incubation temperature up to 24 °C and thereafter it gradually decreases. Peng and co-workers revealed that the high incubation temperature decomposes the aptamer.[85] Therefore 24 °C of the incubation time was used for the entire experiment. This demonstrates the optimum performance of the DNA at room temperature, in accordance with the accompanying safety sheet provided by supplier, Whitehead Scientific (Pty). The analytical performance of the aptasensor on the recognition time of aptamer to OTA was also evaluated as shown in **Figure 4D**. The current response increased with an increasing of the incubation time from 5 to 20 min. When the incubation time was more than 20 min, the current response decreases, suggesting that the bio-recognition reaction was completed. Hence, 20 min of incubation time was chosen. pH value is another significant factor that affects the response of the sensor. Su and co-workers previously reported that an acidic and basic environment could damage the negatively-charged aptamer and therefore affects the interaction

between the aptamer and their targets.[86] The effect of pH on the current response of the C-SPE/rGO/AgNPs/Apt/BSA towards OTA was evaluated at pH 4 to 8 (**Figure S2B**). The current response towards OTA increases until it reaches pH 7 and then it decreases. This result confirms that the aptasensor performance is pH dependent; hence all the electrochemical measurements were conducted at pH 7 to ensure that the fabricated aptasensor functions at its maximum sensitivity.

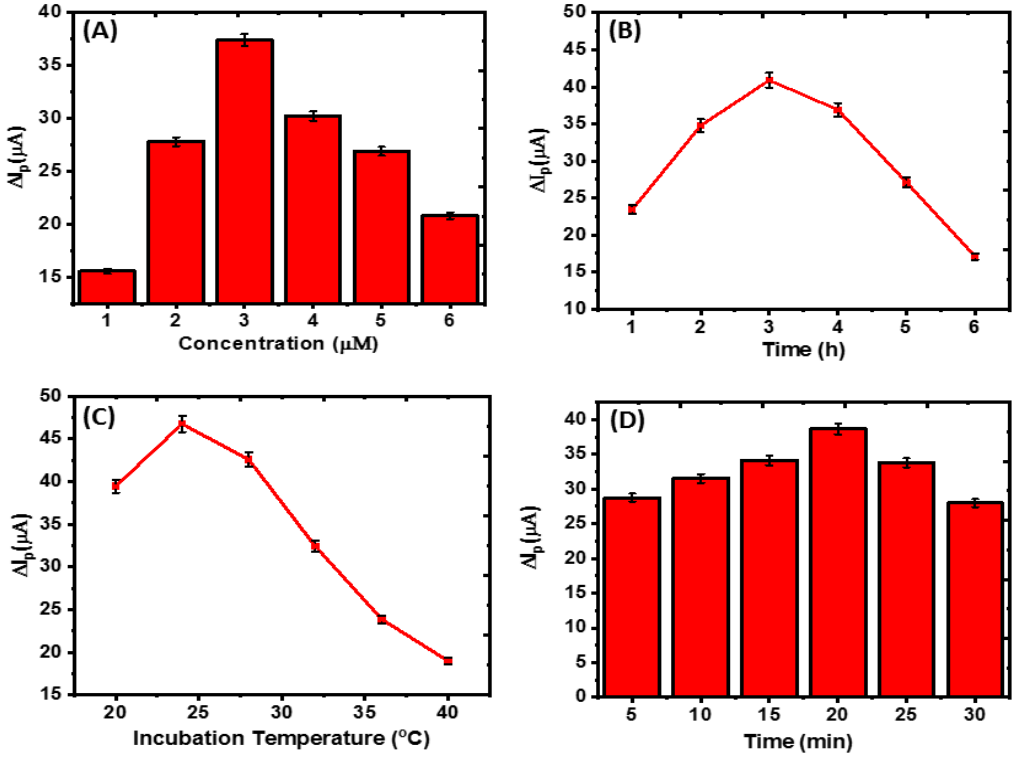

Figure 4. Effect of the aptamer (A) concentration, (B) incubation time, (C) incubation temperature; and (D) Effect of OTA incubation time.

4.1.5 Analytical performance of the fabricated aptasensor

The analytical performance of the fabricated aptasensor was examined by assessing the DPV current response of the aptasensor incubated with OTA concentrations ranging from 0.002 to 0.016 mg/L. **Figure 5A** shows a linearly decreasing peak current with an increasing OTA concentration. This shows that the aptamer was folded and the formation of OTA-Apt complexes on the sensing interface causes inhibition of electron transfer of the redox probe

399 $[Fe(CN)_6]^{3-/4-}$. Quantitative detection of OTA was then carried out by observing the decrease
400 of DPV responses of $[Fe(CN)_6]^{3-/4-}$ peak current by increasing OTA concentration. Under the
401 optimal conditions, the calibration curve of the fabricated aptasensor yielded a linear range
402 from 0.002 to 0.016 mg/L with a correlation coefficient of 0.9968 (**Figure 5B**). The LOD was
403 7×10^{-4} mg/L, and with a similar linear dynamic range observed in previous studies (**Table 1**).

404

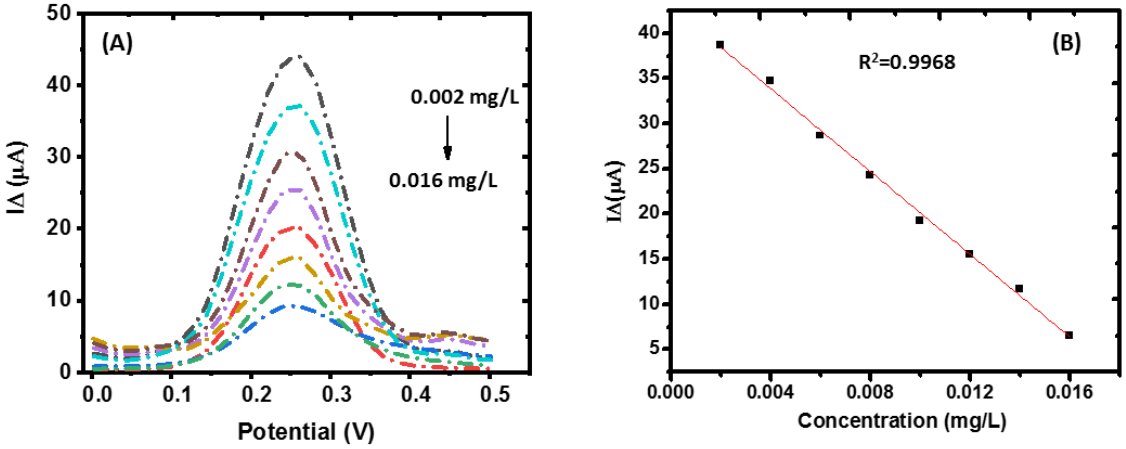

405

406 **Figure 5**. (A) The DPV response of C-SPE/rGO/AgNPs/Apt/BSA in 1 mM $[Fe(CN)_6]^{3-/4-}$ after incubation with
407 different concentrations of OTA from (0.002-0.016 mg/L); and (B) The linear calibration curve of (ΔI_p) with OTA
408 concentrations.

409

Table 1. Comparison of the various reported biosensors for the detection of OTA

Strategy	Sensing Technique	Linear range	LOD	Stability (days)	Reference
Apt/SWCNHs	Fluorescence	20–50 Nm	17.2 nM	-	[87]
dsDNA/PG	Fluorescence	1–1×10^5 ng/mL	1.0 ng/mL	-	[88]
G-quadruplex-ThT/FRET	FRET	5–700 ng/mL	0.4 ng/mL	-	[89]
GCE/CdTe/CS/cDNA/BSA/Cy	(ECL-RET)	5×10^{-4}–50 ng/mL	0.2 pg/mL	5	[90]
5-pDNA	Fluorescent	5–200 ng/mL	1.3 ng/mL	10	[91]
Th–Au octahedral–dsDNA/SA–GR/GCE	Electrochemical	0.001–5 ng/mL	0.1 pg mL	14	[92]
BSA/Apt/AgNPs-rGO/C-SPE	Electrochemical	0.002–0.016 mg/L	7 ×10^{-4} mg/L	20	This work

Single-walled carbon nanohorns **(SWCNHs)**, aptamer **(Apt), double strand (ds)** Deoxyribonucleic acid **(DNA),** Pico Green **(PG),** fluorescence resonance energy transfer **(FRET),** electrochemiluminescence resonance energy transfer **(ECL-RET),** glassy carbon electrode **(GCE),** Cadmium telluride (**CdTe),** chitosan **(CS),** capture DNA **(cDNA),** cyanine dye **(Cy5),** probe DNA **(pDNA),** Bovine serum albumin **(BSA)**, silver nanoparticles **(AgNPs),** reduced graphene oxide **(rGO),** carbon screen printed electrode **(C-SPE)**

4.1.6 Specificity, reproducibility and stability of designed aptasensor

To evaluate the specificity of the proposed aptasensor in response to OTA in the presence of AFB_1, the fabricated aptasensor was incubated in a mixture of 0.002 mg/L and 0.01 mg/L of OTA and AFB_1 respectively. **Figure S3A** shows a major current response when the aptasensor was incubated with 0.002 mg/L of OTA and the mixture, while the incubation of 0.01 mg/L AFB_1 showed a negligible DPV signal, indicating that the fabricated aptasensor is highly specific towards OTA.

The reproducibility of the fabricated aptasensor was studied by the incubation of 0.002 mg/L OTA in six independent aptasensors. The six measurements with a relative standard deviation (RSD) of 3.5% (**Figure S3B**), demonstrating a good reproducibility of the fabricated aptasensor.

In addition, the stability of the aptasensor was evaluated for 20 days. Measurements were recorded at 5-day intervals with an initial current response which decreased to 87.8% (**Figure S3C**), signifying an acceptable stability of the developed aptasensor. The aptasensor was stored in a refrigerator at 4 °C when not in use.

4.1.7 Analytical application of aptasensor

The proposed aptasensor was used for the detection of OTA in Weet-Bix samples. Three OTA standards were added into the extracted samples, with the recoveries ranging from 94.00 to 106.25% (**Table S1**). These results indicate the reliability and the prospective applicability of the proposed aptasensor in food security monitoring.

4.2 Computational Section

In this work, computational modelling was undertaken to better understand the electron transfer capabilities of OTA, computed at the density functional theory (DFT) level as discussed below.

4.2.1 HOMO-LUMO DFT Calculations

Figure 6A-**B** illustrates the HOMO-LUMO plots obtained at the DFT level of theory. Molecular orbitals with the highest energy are considered to be the highest occupied (HOMO) and have the ability to donate electrons. This lower unoccupied molecular orbital (LUMO) informs us that this orbital has an empty electron space, thus suggesting the possibility of acquiring the donated electrons.[93] The calculated energy gap of -4.519 eV supports this greater tendency to donate electrons.

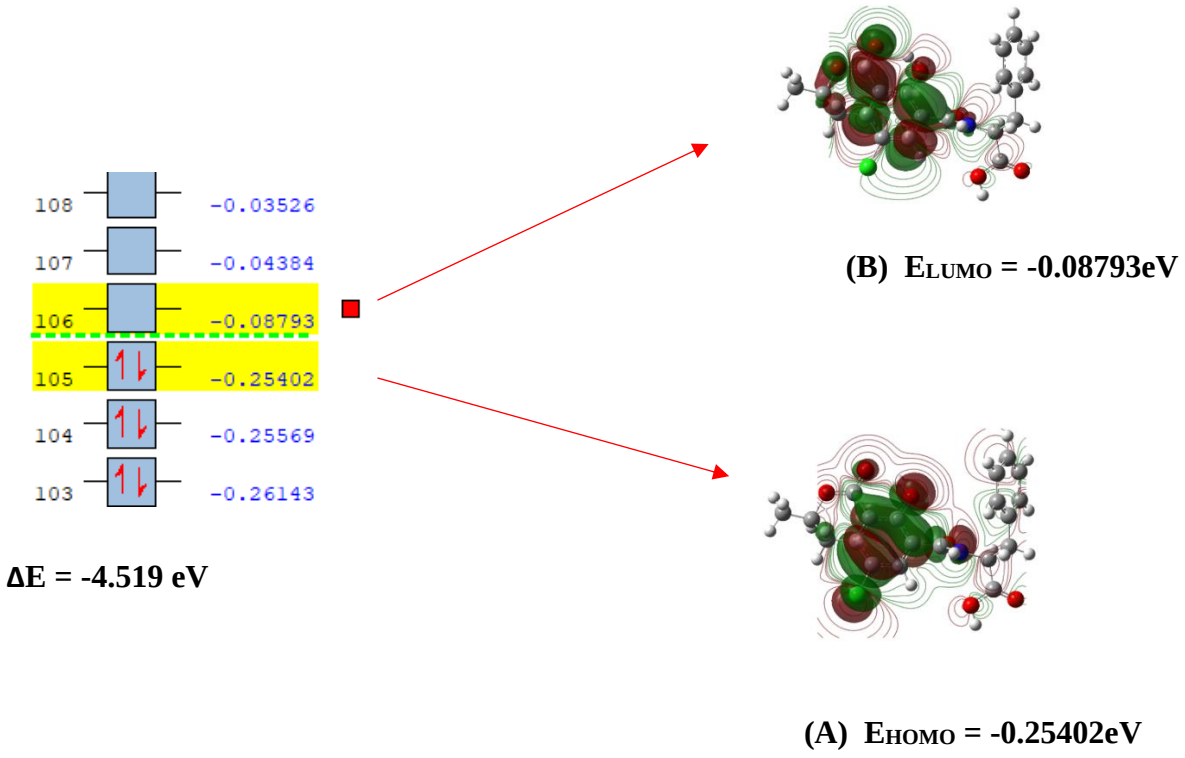

Figure 6. The plots for (A) HOMO, (B) LUMO.

In **Figure 6A**, the electrons located in the highest occupied molecular orbitals (HOMO) orbit around the oxygen atoms in chlorophenolic groups containing dihydro-isocoumarin rings. In accordance with their location, the lowest unoccupied molecular orbitals (LUMO) on chlorophenolic rings have dihydro-isocoumarin rings (**Figure 6B**). According to the results obtained above, carbonyl groups in esters will be a convenient way for electrons to be added to the molecule.

4.2.1 Monte Carlo Adsorption Studies

In this section, we used Monte Carlo simulation methods to calculate the adsorption energies of amorphous adsorbates and substrates to mimic the experimental electrochemical layers **(Scheme 1)**. The adsorption energies for the geometry optimized structures are shown in **Table 2** along with an additional energy decomposition based on the adsorption locator algorithm (**Table S2**).

467 **Table 2. The adsorption energy distributions C-SPE/rGO/AgNPs/Apt/BSA**

Substrate	Adsorbate	optimized 3-D structure	adsorption energy kcal/mol
C-SPE/rGO	AgNPs	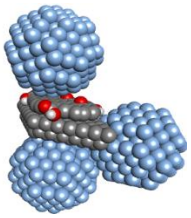 C-SPE/rGO/AgNPs	**-3.1764×10^3**
C-SPE/rGO/AgNPs	Apt	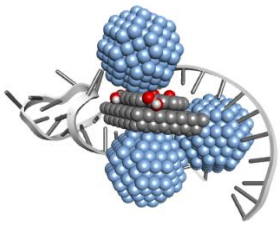 C-SPE/rGO/AgNPs/Apt	**-1.0637×10^3**
C-SPE/rGO/AgNPs/Apt/	BSA	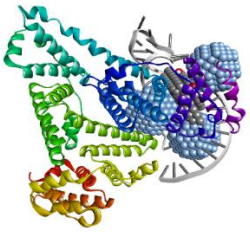 C-SPE/rGO/AgNPs/Apt/BSA	**-198.222**

468

469

Calculated negative adsorption energies indicate stabilization and an exothermic adsorption process.[94, 95] The lower the negative energy, the stronger the adsorption between the adsorbate and substrate. Based on the increase in the anodic peak current observed at E_{pa} = + 0.3V in **Figure 3** (ii) of our nanocomposite, the presence of the aptamer greatly contributes to its stabilization. However, the adsorption energy decreased significantly after BSA was immobilized, as confirmed by a reduction in the peak current (**Figure 3 (iv)**), due to the blocking of the non-specific binding sites of the aptasensor. **Figure 7A** demonstrates the presence of an effective bio-molecular interaction between OTA and the aptamer complex, as it correlates well with the experimental results. A hydrogen bonded interaction between an aptamer and a rGO/AgNPs nanocomposite is shown in **Figure 7B**.

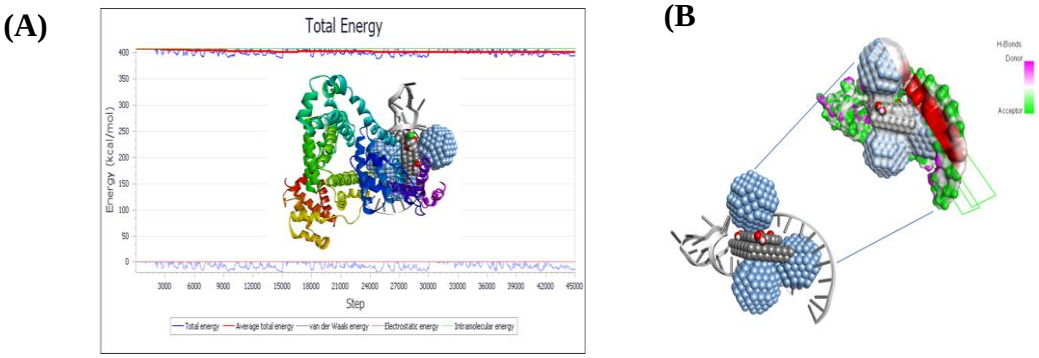

Figure 7. (A) Total energy decomposition plots and 3D representation for SPE/rGO/AgNPs/Apt/BSA-OTA; and (B) the corresponding 3D hydrogen bonded interaction plots for SPE/rGO/AgNPs/Apt.

5. Comparison of experimental data with computational results

The CV for the layer-by-layer electrode fabrication process (**Figure 3** (ii-iv)) demonstrates a linearly decreasing anodic peak current according to the following trend: (ii) C-SPE/rGO/AgNPs > (iii) C-SPE/rGO/AgNPs/Apt > (iv) C-SPE/rGO/AgNPs/Apt/BSA. The corresponding modelled structures obtained from Monte Carlo simulations resulted in an increase in adsorption energy (**Table 2**). This means that the presence of AgNPs fabricated onto C-SPE/rGO nanocomposite is most strongly bound and is attributed to the highly negative adsorption energy (-3.1764 x 10^3 kcal/mol) between the adsorbate-substrate system. Our simulation results indicate that the highly stabilized (C-SPE/rGO/AgNPs) layer is attributed to

the presence of the high energy rGO-AgNPs nanocomposite (**Table S2**), in agreement with the amplified electrochemical signals depicted in **Figure 3** (ii). On the other hand, the presence of the aptamer greatly contributes to a lowering of the peak current (**Figure 3** (iii)) with a corresponding increase in the adsorption energy for the nanocomposite C-SPE/rGO/AgNPs/Apt. Finally, the adsorption energy increased significantly after the immobilization of BSA, with a further decrease in the peak current observed in **Figure 3** (iv). This is attributed to blocking of the non-specific binding sites of the aptasensor as illustrated in **Figure 7A-B**. Clearly, the highly negative adsorption energy observed when OTA interacted with the C-SPE/rGO/AgNPs/Apt/BSA, demonstrates the existence of a good bio-molecular interaction between OTA and the aptamer complex which correlates well with the experimental results.

6. Conclusions

The purpose of this study was to develop an electrochemical aptasensor capable of detecting OTA in commercial Weet-Bix samples with high sensitivity and efficiency. With a combination of experimental and computational techniques, we demonstrated that the nanocomposite construction utilizing rGO and AgNP and OTA detector provided good sensitivity, were easy to use, and were cost effective. Further, all the techniques utilized in this study allowed simultaneous morphological and size analyses. It can be concluded that AF4-MALS, spICP-MS, and TEM analyses are accurately inferring the presence of nanoparticles. According to AF4-MALS analysis, the geometric diameter of AgNPs was 55 nm, while the mean particle size distribution diameter was 48 nm, and the core size was 53 nm in TEM analysis. Furthermore, the images obtained by TEM confirmed that the synthesized AgNPs were spherical in shape. Using the proposed aptasensor, the concentration range was enhanced from 0.002 to 0.016 mg/L with an LOD of 7×10^{-4} mg/L. Moreover, the presence of AFB_1 did not show any significant changes in the current. Ample evidence of the effectiveness of the proposed aptasensor system was obtained when Weet-Bix samples were spiked. A good recovery was obtained with an acceptable range (94.00 to 106.25%).

The use of computational modeling has also provided structural information about interactions between biomolecules and nanostructures, as well as electronic properties of OTA. Electrochemically modified aptasensors show good agreement with computed adsorption energies and current responses. Weet-Bix samples can be detected by the proposed aptasensor using disposable C-SPEs on-site using the disposable C-SPEs.

Conflict of interest

The authors declare that there is no conflict of interest regarding the publication of this manuscript.

Acknowledgements

This work was financially supported by Council for Scientific and Industrial Research (CSIR), (South Africa). We also acknowledge financial support from the French Embassy Scholarship from South Africa.

Supporting Information

Graphical representation of OTA, amadumbe image, HR-TEM image for AgNPs, reduction of AgNPs, graphical representation of the rGO: AgNPs, representation of pH on change in peak currents, graphical representation of specificity of the aptasensor in AFB_1, representation of reproducibility of the aptasensor with independent electrodes, representation of the storage stability of the OTA aptasensor, tabulated recoveries of OTA, tabulated energy decomposition.

7. References

1. Abnous, K.; Danesh, N. M.; Alibolandi, M.; Ramezani, M.; Taghdisi, S. M., Amperometric aptasensor for ochratoxin A based on the use of a gold electrode modified with aptamer, complementary DNA, SWCNTs and the redox marker Methylene Blue. *Microchimica Acta* **2017,** *184* (4), 1151-1159.

2. Sánchez-Montero, L.; Córdoba, J. J.; Peromingo, B.; Álvarez, M.; Núñez, F., Effects of environmental conditions and substrate on growth and ochratoxin A production by Penicillium verrucosum and Penicillium nordicum: Relative risk assessment of OTA in dry-cured meat products. *Food Research International* **2019,** *121*, 604-611.

3. Paola, B.; Marco, C. L., OTA-grapes: a mechanistic model to predict ochratoxin A risk in grapes, a step beyond the systems approach. *Toxins* **2015,** *7* (8), 3012-3029.

4. Jalili, M., Natural occurrence of ochratoxin A contamination in commercial spices in Tehran. *Nutrition and Food Sciences Research* **2016,** *3* (3), 25-30.

5. Qi, L.; Li, Y.; Luo, X.; Wang, R.; Zheng, R.; Wang, L.; Li, Y.; Yang, D.; Fang, W.; Chen, Z., Detoxification of zearalenone and ochratoxin A by ozone and quality evaluation of ozonised corn. *Food Additives & Contaminants: Part A* **2016,** *33* (11), 1700-1710.

6. Liu, L.; Xu, L.; Suryoprabowo, S.; Song, S.; Kuang, H., Development of an immunochromatographic test strip for the detection of ochratoxin A in red wine. *Food and Agricultural Immunology* **2018,** *29* (1), 434-444.

7. Pei, K.; Xiong, Y.; Li, X.; Jiang, H.; Xiong, Y., Colorimetric ELISA with an acid–base indicator for sensitive detection of ochratoxin A in corn samples. *Analytical Methods* **2018,** *10* (1), 30-36.

8. Chebil, S.; Oueslati, S.; Ben-Amar, A.; Natskoulis, P., Ochratoxigenic fungi and Ochratoxin A determination in dried grapes marketed in Tunisia. *Annals of Microbiology* **2020,** *70* (1), 1-9.

9. Kunene, K.; Weber, M.; Sabela, M.; Voiry, D.; Kanchi, S.; Bisetty, K.; Bechelany, M., Highly-efficient electrochemical label-free immunosensor for the detection of ochratoxin A in coffee samples. *Sensors and Actuators B: Chemical* **2020,** *305*, 127438.

10. Welke, J. E., Fungal and mycotoxin problems in grape juice and wine industries. *Current Opinion in Food Science* **2019,** *29*, 7-13.

11. Cappozzo, J.; Jackson, L.; Lee, H. J.; Zhou, W.; Al-Taher, F.; Zweigenbaum, J.; Ryu, D., Occurrence of ochratoxin A in infant foods in the United States. *Journal of food protection* **2017,** *80* (2), 251-256.

12. Heshmati, A.; Zohrevand, T.; Khaneghah, A. M.; Nejad, A. S. M.; Sant'Ana, A. S., Co-occurrence of aflatoxins and ochratoxin A in dried fruits in Iran: Dietary exposure risk assessment. *Food and Chemical Toxicology* **2017,** *106*, 202-208.

13. Jedidi, I.; Cruz, A.; González-Jaén, M. T.; Said, S., Aflatoxins and ochratoxin A and their Aspergillus causal species in Tunisian cereals. *Food Additives & Contaminants: Part B* **2017,** *10* (1), 51-58.

14. Sun, Z.; Wang, X.; Tang, Z.; Chen, Q.; Liu, X., Development of a biotin-streptavidin-amplified nanobody-based ELISA for ochratoxin A in cereal. *Ecotoxicology and environmental safety* **2019,** *171*, 382-388.

15. Khaneghah, A. M.; Fakhri, Y.; Abdi, L.; Coppa, C. F. S. C.; Franco, L. T.; de Oliveira, C. A. F., The concentration and prevalence of ochratoxin A in coffee and coffee-based products: A global systematic review, meta-analysis and meta-regression. *Fungal biology* **2019,** *123* (8), 611-617.

16. Leal, T.; Abrunhosa, L.; Domingues, L.; Venâncio, A.; Oliveira, C., BSA-based sample clean-up columns for ochratoxin A determination in wine: Method development and validation. *Food chemistry* **2019,** *300*, 125204.

17. Lhotská, I.; Šatínský, D.; Havlíková, L.; Solich, P., A fully automated and fast method using direct sample injection combined with fused-core column on-line SPE–HPLC for determination of ochratoxin A and citrinin in lager beers. *Analytical and bioanalytical chemistry* **2016,** *408* (12), 3319-3329.

18. Casoni, D.; Badea, M.; Bros, I.; Cobzac, S. C. A., Investigation on image processing parameters for plate evaluation in TLC analysis of mycotoxins. *Stud. Univ. Babe? Bolyai Chem* **2017,** *62*, 89-102.

19. Elaridi, J.; Yamani, O.; Al Matari, A.; Dakroub, S.; Attieh, Z., Determination of ochratoxin A (OTA), ochratoxin B (OTB), T-2, and HT-2 toxins in wheat grains, wheat flour, and bread in Lebanon by LC-MS/MS. *Toxins* **2019,** *11* (8), 471.

20. Zhang, X.; Li, M.; Cheng, Z.; Ma, L.; Zhao, L.; Li, J., A comparison of electronic nose and gas chromatography–mass spectrometry on discrimination and prediction of ochratoxin A content in Aspergillus carbonarius cultured grape-based medium. *Food chemistry* **2019,** *297*, 124850.

21. Fadlalla, M. H.; Ling, S.; Wang, R.; Li, X.; Yuan, J.; Xiao, S.; Wang, K.; Tang, S.; Elsir, H.; Wang, S., Development of ELISA and Lateral Flow Immunoassays for Ochratoxins (OTA and OTB) Detection Based on Monoclonal Antibody. *Frontiers in cellular and infection microbiology* **2020,** *10*, 80.

22. Röthlisberger, P.; Hollenstein, M., Aptamer chemistry. *Advanced drug delivery reviews* **2018,** *134*, 3-21.

23. Wang, L.; Ma, W.; Chen, W.; Liu, L.; Ma, W.; Zhu, Y.; Xu, L.; Kuang, H.; Xu, C., An aptamer-based chromatographic strip assay for sensitive toxin semi-quantitative detection. *Biosensors and Bioelectronics* **2011,** *26* (6), 3059-3062.

24. Hao, N.; Jiang, L.; Qian, J.; Wang, K., Ultrasensitive electrochemical Ochratoxin A aptasensor based on CdTe quantum dots functionalized graphene/Au nanocomposites and magnetic separation. *Journal of Electroanalytical Chemistry* **2016,** *781*, 332-338.

25. He, Y.; Tian, F.; Zhou, J.; Jiao, B., A fluorescent aptasensor for ochratoxin A detection based on enzymatically generated copper nanoparticles with a polythymine scaffold. *Microchimica Acta* **2019,** *186* (3), 1-7.

26. Tian, F.; Zhou, J.; Jiao, B.; He, Y., A nanozyme-based cascade colorimetric aptasensor for amplified detection of ochratoxin A. *Nanoscale* **2019,** *11* (19), 9547-9555.

27. Yan, X.-L.; Xue, X.-X.; Luo, J.; Jian, Y.-T.; Tong, L.; Zheng, X.-J., Construction of chemiluminescence aptasensor platform using magnetic microsphere for ochratoxin A detection based on G bases derivative reaction and Au NPs catalyzing luminol system. *Sensors and Actuators B: Chemical* **2020,** *320*, 128375.

28. Taghdisi, S. M.; Danesh, N. M.; Ramezani, M.; Alibolandi, M.; Nameghi, M. A.; Gerayelou, G.; Abnous, K., A novel electrochemical aptasensor for ochratoxin a sensing in spiked food using strand-displacement polymerase reaction. *Talanta* **2021,** *223*, 121705.

29. Liu, S.; Wang, Y.; Xu, W.; Leng, X.; Wang, H.; Guo, Y.; Huang, J., A novel sandwich-type electrochemical aptasensor based on GR-3D Au and aptamer-AuNPs-HRP for sensitive detection of oxytetracycline. *Biosensors and Bioelectronics* **2017,** *88*, 181-187.

30. Zeng, R.; Su, L.; Luo, Z.; Zhang, L.; Lu, M.; Tang, D., Ultrasensitive and label-free electrochemical aptasensor of kanamycin coupling with hybridization chain reaction and strand-displacement amplification. *Analytica chimica acta* **2018,** *1038*, 21-28.

31. Lv, L.; Wang, X., Recent advances in ochratoxin A electrochemical biosensors: Recognition elements, sensitization technologies, and their applications. *Journal of agricultural and food chemistry* **2020,** *68* (17), 4769-4787.

32. Sang, S.; Li, D.; Zhang, H.; Sun, Y.; Jian, A.; Zhang, Q.; Zhang, W., Facile synthesis of AgNPs on reduced graphene oxide for highly sensitive simultaneous detection of heavy metal ions. *RSC advances* **2017,** *7* (35), 21618-21624.

33. Wei, L.; Lu, J.; Xu, H.; Patel, A.; Chen, Z.-S.; Chen, G., Silver nanoparticles: synthesis, properties, and therapeutic applications. *Drug discovery today* **2015,** *20* (5), 595-601.

34. Shetti, N. P.; Nayak, D. S.; Reddy, K. R.; Aminabhvi, T. M., Graphene–clay-based hybrid nanostructures for electrochemical sensors and biosensors. In *Graphene-Based Electrochemical Sensors for Biomolecules*, Elsevier: 2019; pp 235-274.

35. Zhou, Y.; Fang, Y.; Ramasamy, R. P., Non-covalent functionalization of carbon nanotubes for electrochemical biosensor development. *Sensors* **2019,** *19* (2), 392.

36. Pan, M.; Yang, J.; Liu, K.; Yin, Z.; Ma, T.; Liu, S.; Xu, L.; Wang, S., Noble metal nanostructured materials for chemical and biosensing systems. *Nanomaterials* **2020,** *10* (2), 209.

37. Xuan, X.; Yoon, H. S.; Park, J. Y., A wearable electrochemical glucose sensor based on simple and low-cost fabrication supported micro-patterned reduced graphene oxide nanocomposite electrode on flexible substrate. *Biosensors and Bioelectronics* **2018,** *109*, 75-82.

38. Ladrón-de-Guevara, A.; Boscá, A.; Pedrós, J.; Climent-Pascual, E.; De Andrés, A.; Calle, F.; Martínez, J., Reduced graphene oxide/polyaniline electrochemical supercapacitors fabricated by laser. *Applied Surface Science* **2019,** *467*, 691-697.

39. Srivastava, S.; Kumar, V.; Arora, K.; Singh, C.; Ali, M. A.; Puri, N. K.; Malhotra, B. D., Antibody conjugated metal nanoparticle decorated graphene sheets for a mycotoxin sensor. *RSC advances* **2016,** *6* (61), 56518-56526.

40. Shukla, S.; Haldorai, Y.; Khan, I.; Kang, S.-M.; Kwak, C. H.; Gandhi, S.; Bajpai, V. K.; Huh, Y. S.; Han, Y.-K., Bioreceptor-free, sensitive and rapid electrochemical detection of patulin fungal toxin, using a reduced graphene oxide@ SnO2 nanocomposite. *Materials Science and Engineering: C* **2020,** *113*, 110916.

41. Jiang, L.; Qian, J.; Yang, X.; Yan, Y.; Liu, Q.; Wang, K.; Wang, K., Amplified impedimetric aptasensor based on gold nanoparticles covalently bound graphene sheet for the picomolar detection of ochratoxin A. *Analytica chimica acta* **2014,** *806*, 128-135.

42. Modi, A. T., Effect of indigenous storage method on performance of taro [Colocasia esculenta (L.) Schott] under field conditions in a warm subtropical area. *South African Journal of Plant and Soil* **2007,** *24* (4), 214-219.

43. Zhang, J.; Xu, X.; Qiang, Y., Ultrasensitive electrochemical aptasensor for ochratoxin A detection using AgPt bimetallic nanoparticles decorated iron-porphyrinic metal-organic framework for signal amplification. *Sensors and Actuators B: Chemical* **2020,** *312*, 127964.

44. Guerrero-Contreras, J.; Caballero-Briones, F., Graphene oxide powders with different oxidation degree, prepared by synthesis variations of the Hummers method. *Materials Chemistry and Physics* **2015,** *153*, 209-220.

45. Zaaba, N.; Foo, K.; Hashim, U.; Tan, S.; Liu, W.-W.; Voon, C., Synthesis of graphene oxide using modified hummers method: solvent influence. *Procedia engineering* **2017,** *184*, 469-477.

46. Ye, Y.; Ding, S.; Ye, Y.; Xu, H.; Cao, X.; Liu, S.; Sun, H., Enzyme-based sensing of glucose using a glassy carbon electrode modified with a one-pot synthesized nanocomposite consisting of chitosan, reduced graphene oxide and gold nanoparticles. *Microchimica Acta* **2015,** *182* (9), 1783-1789.

47. Tamileswari, R.; Nisha, M. H.; Jesurani, S.; Kanagesan, S.; Hashim, M.; Catherine, S.; Alexander, P., Synthesis of silver nanoparticles using the vegetable extract of Raphanus sativus (radish) and assessment of their antibacterial activity. *Int. J. Adv. Technol. Eng. Sci* **2015,** *3*, 207-212.

48. Rivas, L.; Mayorga-Martinez, C. C.; Quesada-González, D.; Zamora-Gálvez, A.; de la Escosura-Muñiz, A.; Merkoçi, A., Label-free impedimetric aptasensor for ochratoxin-A detection using iridium oxide nanoparticles. *Analytical chemistry* **2015,** *87* (10), 5167-5172.

49. He, Q.-H.; Xu, Y.; Wang, D.; Kang, M.; Huang, Z.-B.; Li, Y.-P., Simultaneous multiresidue determination of mycotoxins in cereal samples by polyvinylidene fluoride membrane based dot immunoassay. *Food chemistry* **2012,** *134* (1), 507-512.

50. Naidoo, L.; Kanchi, S.; Drexel, R.; Meier, F.; Bisetty, K., Measurement of TiO2 Nanoscale Ingredients in Sunscreens by Multidetector AF4, TEM, and spICP-MS Supported by Computational Modeling. *ACS Applied Nano Materials* **2021,** *4* (5), 4665-4675.

51. Kim, S. T.; Kim, H. K.; Han, S. H.; Jung, E. C.; Lee, S., Determination of size distribution of colloidal TiO2 nanoparticles using sedimentation field-flow fractionation combined with single particle mode of inductively coupled plasma-mass spectrometry. *Microchemical Journal* **2013,** *110*, 636-642.

52. Laborda, F.; Jiménez-Lamana, J.; Bolea, E.; Castillo, J. R., Critical considerations for the determination of nanoparticle number concentrations, size and number size distributions by single particle ICP-MS. *Journal of Analytical Atomic Spectrometry* **2013,** *28* (8), 1220-1232.

53. Yang, Y.; Long, C.-L.; Yang, Z.-G.; Li, H.-P.; Wang, Q., Characterization and Determination of Silver Nanoparticle Using Single Particle-Inductively Coupled Plasma-Mass Spectrometry. *Chinese Journal of Analytical Chemistry* **2014,** *42* (11), 1553-1560.

54. Bisetty, K.; Kanchi, S.; Hloma, P., Evaluation of the catalytic activity of graphene oxide and zinc oxide nanoparticles on the electrochemical sensing of T1R2-Rebaudioside A complex supported by in silico methods. *Pure and Applied Chemistry* **2021**.

55. Frisch, M.; Trucks, G.; Schlegel, H.; Scuseria, G.; Robb, M.; Cheeseman, J.; Scalmani, G.; Barone, V.; Petersson, G.; Nakatsuji, H., Gaussian 16 revision a. 03. 2016; gaussian inc. *Wallingford CT* **2016,** *2* (4).

56. Naidoo, L.; Suvardhan, K.; Sabela, M. I.; Bisetty, K., Multivariate optimization of field-flow fractionation of nanoscale synthetic amorphous silica in processed foods supported by computational modelling. *New Journal of Chemistry* **2020,** *44* (40), 17542-17551.

57. Sun, H., COMPASS: an ab initio force-field optimized for condensed-phase applications overview with details on alkane and benzene compounds. *The Journal of Physical Chemistry B* **1998,** *102* (38), 7338-7364.

58. Jeddi, I.; Saiz, L., Three-dimensional modeling of single stranded DNA hairpins for aptamer-based biosensors. *Scientific reports* **2017,** *7* (1), 1-13.

59. Ulicny, J.; Kozar, T. In *Roadmap for Computer-Aided Modeling of Theranostics and Related Nanosystems*, EPJ Web of Conferences, EDP Sciences: 2018; p 05017.

60. Veisi, H.; Azizi, S.; Mohammadi, P., Green synthesis of the silver nanoparticles mediated by Thymbra spicata extract and its application as a heterogeneous and recyclable nanocatalyst for catalytic reduction of a variety of dyes in water. *Journal of cleaner production* **2018,** *170*, 1536-1543.

61. Ahmed, S.; Ahmad, M.; Swami, B. L.; Ikram, S., A review on plants extract mediated sythesis of silver nanoparticles for antimicrobial applications: a green expertise. *Journal of advanced research* **2016,** *7* (1), 17-28.

62. Kathiravan, V.; Ravi, S.; Ashokkumar, S., Synthesis of silver nanoparticles from Melia dubia leaf extract and their in vitro anticancer activity. *Spectrochimica Acta Part A: Molecular and Biomolecular Spectroscopy* **2014,** *130*, 116-121.

63. Ndikau, M.; Noah, N. M.; Andala, D. M.; Masika, E., Green synthesis and characterization of silver nanoparticles using Citrullus lanatus fruit rind extract. *International Journal of Analytical Chemistry* **2017,** *2017*.

64. Alsharif, S. M.; Salem, S. S.; Abdel-Rahman, M. A.; Fouda, A.; Eid, A. M.; Hassan, S. E.-D.; Awad, M. A.; Mohamed, A. A., Multifunctional properties of spherical silver nanoparticles fabricated by different microbial taxa. *Heliyon* **2020,** *6* (5), e03943.

65. Krishna, R.; Titus, E.; Okhay, O.; Gil, J. C.; Ventura, J.; Ramana, E. V.; Gracio, J. J., Rapid electrochemical synthesis of hydrogenated graphene oxide using Ni nanoparticles. *Int. J. Electrochem. Sci* **2014,** *9*, 4054-4069.

66. Emiru, T. F.; Ayele, D. W., Controlled synthesis, characterization and reduction of graphene oxide: A convenient method for large scale production. *Egyptian Journal of Basic and Applied Sciences* **2017,** *4* (1), 74-79.

67. Hidayah, N.; Liu, W.-W.; Lai, C.-W.; Noriman, N.; Khe, C.-S.; Hashim, U.; Lee, H. C. In *Comparison on graphite, graphene oxide and reduced graphene oxide: Synthesis and characterization*, AIP Conference Proceedings, AIP Publishing LLC: 2017; p 150002.

68. Roy, I.; Sarkar, G.; Mondal, S.; Rana, D.; Bhattacharyya, A.; Saha, N. R.; Adhikari, A.; Khastgir, D.; Chattopadhyay, S.; Chattopadhyay, D., Synthesis and characterization of graphene from waste dry cell battery for electronic applications. *RSC advances* **2016,** *6* (13), 10557-10564.

69. Gebreegziabher, G.; Asemahegne, A.; Ayele, D.; Dhakshnamoorthy, M.; Kumar, A., One-step synthesis and characterization of reduced graphene oxide using chemical exfoliation method. *Materials Today Chemistry* **2019,** *12*, 233-239.

70. Xu, C.; Shi, X.; Ji, A.; Shi, L.; Zhou, C.; Cui, Y., Fabrication and characteristics of reduced graphene oxide produced with different green reductants. *PloS one* **2015,** *10* (12), e0144842.

71. Husnah, M.; Fakhri, H. A.; Rohman, F.; Aimon, A. H.; Iskandar, F., A modified Marcano method for improving electrical properties of reduced graphene oxide (rGO). *Materials Research Express* **2017,** *4* (6), 064001.

72. Iskandar, F.; Hikmah, U.; Stavila, E.; Aimon, A. H., Microwave-assisted reduction method under nitrogen atmosphere for synthesis and electrical conductivity improvement of reduced graphene oxide (rGO). *RSC advances* **2017,** *7* (83), 52391-52397.

73. Malas, A.; Bharati, A.; Verkinderen, O.; Goderis, B.; Moldenaers, P.; Cardinaels, R., Effect of the GO reduction method on the dielectric properties, electrical conductivity and crystalline behavior of PEO/rGO nanocomposites. *Polymers* **2017,** *9* (11), 613.

74. He, D.; Peng, Z.; Gong, W.; Luo, Y.; Zhao, P.; Kong, L., Mechanism of a green graphene oxide reduction with reusable potassium carbonate. *RSC advances* **2015,** *5* (16), 11966-11972.

75. Gülercan, D.; Gergin, İ.; Sarac, A. S., Preparation and Electrochemical Performances of graphene oxide/PEDOT and reduced graphene oxide/PEDOT nanofibers and nanocomposites. *Fibers and Polymers* **2018,** *19* (10), 2178-2187.

76. Thangavel, P.; Kannan, R.; Ramachandran, B.; Moorthy, G.; Suguna, L.; Muthuvijayan, V., Development of reduced graphene oxide (rGO)-isabgol nanocomposite

783 dressings for enhanced vascularization and accelerated wound healing in normal and diabetic
784 rats. *Journal of colloid and interface science* **2018,** *517*, 251-264.

785 77. Johra, F. T.; Jung, W.-G., Hydrothermally reduced graphene oxide as a supercapacitor.
786 *Applied Surface Science* **2015,** *357*, 1911-1914.

787 78. Yuan, Y.-G.; Gurunathan, S., Combination of graphene oxide–silver nanoparticle
788 nanocomposites and cisplatin enhances apoptosis and autophagy in human cervical cancer
789 cells. *International Journal of Nanomedicine* **2017,** *12*, 6537.

790 79. Bagheri, R.; Karimzadeh, F.; Kermanpur, A.; Kharaziha, M., The novel
791 immobilization of G-quadruplex aptamer on Cu deposited surface using electrochemical
792 method. *Materials Letters* **2021,** *282*, 128703.

793 80. Gurunathan, S.; Hyun Park, J.; Choi, Y.-J.; Woong Han, J.; Kim, J.-H., Synthesis of
794 graphene oxide-silver nanoparticle nanocomposites: an efficient novel antibacterial agent.
795 *Current Nanoscience* **2016,** *12* (6), 762-773.

796 81. Yang, B.; Liu, Z.; Guo, Z.; Zhang, W.; Wan, M.; Qin, X.; Zhong, H., In situ green
797 synthesis of silver–graphene oxide nanocomposites by using tryptophan as a reducing and
798 stabilizing agent and their application in SERS. *Applied surface science* **2014,** *316*, 22-27.

799 82. Aydogdu, G.; Pekyardimci, S., An electrochemical sandwich-type aptasensor for
800 determination of lipocalin-2 based on graphene oxide/ polymer composite and gold
801 nanoparticles. . *Talanta* **2020,** *210* (120666).

802 83. Liu, S.; Xing, X.; Yu, J.; Lian, W.; Li, J.; Cui, M.; Huang, J., A novel label-free
803 electrochemical aptasensor based on graphene–polyaniline composite film for dopamine
804 determination. *Biosensors and Bioelectronics* **2012,** *36* (1), 186-191.

805 84. Bojang, A. A.; Wu, H. S., Characterization of electrode performance in enzymatic
806 biofuel cells using cyclic voltammetry and electrochemical impedance spectroscopy. *Catalysts*
807 **2020,** *10* (7), 782.

808 85. Peng, H.; Hui, Y.; Ren, R.; Wang, B.; Song, S.; He, Y.; Zhang, F., A sensitive
809 electrochemical aptasensor based on MB-anchored GO for the rapid detection of Cronobacter
810 sakazakii. *Journal of Solid State Electrochemistry* **2019,** *23* (12), 3391-3398.

811 86. Su, W.; Kim, S.-E.; Cho, M.; Nam, J.-D.; Choe, W.-S.; Lee, Y., Selective detection
812 of endotoxin using an impedance aptasensor with electrochemically deposited gold
813 nanoparticles. *Innate immunity* **2013,** *19* (4), 388-397.

814 87. Lv, L.; Cui, C.; Liang, C.; Quan, W.; Wang, S.; Guo, Z., Aptamer-based single-
815 walled carbon nanohorn sensors for ochratoxin A detection. *Food Control* **2016,** *60*, 296-301.

816 88. Lv, Z.; Chen, A.; Liu, J.; Guan, Z.; Zhou, Y.; Xu, S.; Yang, S.; Li, C., A simple and
817 sensitive approach for ochratoxin A detection using a label-free fluorescent aptasensor. *PloS*
818 *one* **2014,** *9* (1), e85968.

819 89. Zeng, H.; Zhu, Y.; Ma, L.; Xia, X.; Li, Y.; Ren, Y.; Zhao, W.; Yang, H.; Deng, R.,
820 G-quadruplex specific dye-based ratiometric FRET aptasensor for robust and ultrafast
821 detection of toxin. *Dyes and Pigments* **2019,** *164*, 35-42.

822 90. Gao, J.; Chen, Z.; Mao, L.; Zhang, W.; Wen, W.; Zhang, X.; Wang, S.,
823 Electrochemiluminescent aptasensor based on resonance energy transfer system between CdTe
824 quantum dots and cyanine dyes for the sensitive detection of Ochratoxin A. *Talanta* **2019,** *199*,
825 178-183.

826 91. Costantini, F.; Lovecchio, N.; Ruggi, A.; Manetti, C.; Nascetti, A.; Reverberi, M.;
827 de Cesare, G.; Caputo, D., Fluorescent Label-Free Aptasensor Integrated in a Lab-on-Chip
828 System for the Detection of Ochratoxin A in Beer and Wheat. *ACS Applied Bio Materials* **2019,**
829 *2* (12), 5880-5887.

830 92. Wei, M.; Yue, S.; Zhang, W.; Li, X., Development of an electrochemical aptasensor
831 using Au octahedra and graphene for signal amplification. *Analytical Methods* **2020,** *12* (3),
832 317-323.

833 93. Kanchi, S.; Sabela, M.; Singh, P.; Bisetty, K., Multivariate optimization of differential
834 pulse polarographic–catalytic hydrogen wave technique for the determination of nickel (II) in
835 real samples. *Arabian Journal of Chemistry* **2017,** *10*, S2260-S2272.

836 94. Arya, M.; Niklasson, J.; Mohsenzadeh, A.; Bolton, K., A density functional theory
837 study of reactions of relevance to catalytic hydrocarbon synthesis and combustion. *Theoretical*
838 *Chemistry Accounts* **2018,** *137* (11), 1-14.

839 95. Putri, A. D.; Murti, B. T.; Kanchi, S.; Sabela, M. I.; Bisetty, K.; Tiwari, A.; Asiri,
840 A. M., Computational studies on the molecular insights of aptamer induced poly (N-
841 isopropylacrylamide)-graft-graphene oxide for on/off-switchable whole-cell cancer
842 diagnostics. *Scientific reports* **2019,** *9* (1), 1-14.

843